RSC Advances

PAPER

View Article Online
View Journal | View Issue

Cite this: *RSC Adv.*, 2025, **15**, 44883

Mechanistic insights into the role of alkali metal activation in CO_2 adsorption by nitrogen-doped coal-based carbon materials

Zeru Gong,[ab] Liang Xie,[c] Wanjing Li,[c] Huijun Situ,[c] Pu Liu,[c] Wei Zhou [c] and Xiaoxiao Meng *[c]

Nitrogen-doped coal-based carbon materials have attracted significant attention in the field of CO_2 capture due to their low cost, high specific surface area, and tunable surface chemistry. However, the mechanism by which alkali metal activation (*e.g.*, K/Na) influences CO_2 adsorption performance remains unclear, particularly regarding the synergistic effects between alkali metals and nitrogen species, as well as their impact on the electronic structure. In this study, density functional theory (DFT) was employed to systematically investigate the synergistic mechanisms between alkali metal activation (K, Na) and typical nitrogen doping configurations—pyridinic-N, pyrrolic-N, graphitic-N, and amine-N—on CO_2 adsorption performance in coal-based carbon materials. By constructing and optimizing C–O–M (M = K, Na) structures co-doped with nitrogen, we calculated the CO_2 adsorption energies and analyzed the corresponding electronic characteristics. The results show that the formation of C–O–M structures significantly enhances CO_2 adsorption capacity: Na-doped (−35.88 kJ mol^{-1}) and K-doped (−31.72 kJ mol^{-1}) systems exhibit much higher adsorption strengths than nitrogen-only doped counterparts (−17 to −13 kJ mol^{-1}). Further analysis of weak interactions revealed that alkali metals generate regions of high electrostatic potential on the carbon surface (at K/Na sites), while pyridinic-N introduces low-potential zones, thereby forming a strong electrostatic gradient field. This study uncovers the electronic role of alkali metals beyond their traditional function as pore-forming agents and highlights the dominant contribution of electrostatic interactions in CO_2 adsorption. These findings provide theoretical guidance for the synergistic optimization of pore structure and surface chemistry, promoting the rational design of high-performance coal-based CO_2 adsorbents.

Received 28th August 2025
Accepted 3rd November 2025

DOI: 10.1039/d5ra06428g

rsc.li/rsc-advances

1. Introduction

The excessive emission of greenhouse gases has significantly altered the composition of the Earth's atmosphere, leading to the intensification of the greenhouse effect. This phenomenon has triggered a cascade of environmental issues, including global temperature rise, climate change, and a variety of associated ecological impacts.[1] Among the major greenhouse gases, carbon dioxide (CO_2) exhibits a particularly strong correlation with the increase in global surface temperatures.[2,3] Since the onset of the industrial era, atmospheric CO_2 concentrations have risen dramatically—from approximately 280 parts per million (ppm) to over 400 ppm.[4,5] To mitigate this trend, two primary strategies can be employed: controlling emissions at the source (preventing CO_2 generation) and capturing CO_2 at the end-of-pipe stage (post-combustion capture). Notably, fossil fuel combustion accounts for approximately 88% of anthropogenic greenhouse gas emissions. However, given current global energy demands, the complete elimination of fossil fuels remains unfeasible in the short term. Therefore, effective capture and sequestration of CO_2 emissions at the tail end of industrial processes is essential for mitigating climate change and easing its environmental consequences.[6]

Numerous materials and technologies have been developed for carbon dioxide (CO_2) capture, including solid adsorbents such as metal–organic frameworks (MOFs),[7] zeolites,[8] and carbon-based materials.[9,10] Among them, coal-derived carbon materials have garnered increasing attention due to their low cost, tunable structure, and ease of processing.[10] For coal-based carbon materials, heteroatom doping—particularly nitrogen—can effectively modulate the electronic structure and enhance the adsorption capacity of active sites for CO_2.[11,12] Additionally, activation with alkali metals significantly increases the pore volume and specific surface area of the carbon matrix, thereby improving the density and accessibility of active sites and

[a]*Department of Energy and Power Engineering, Tsinghua University, Beijing 100084, People's Republic of China*
[b]*China Energy Investment Group Guangdong Power Co., Ltd, Guangzhou 510710, People's Republic of China*
[c]*School of Energy Science and Engineering, Harbin Institute of Technology, Harbin 150001, People's Republic of China. E-mail: mengxiaoxiao@hit.edu.cn*

further enhancing CO_2 uptake.[13,14] These strategies have demonstrated strong practical applicability. For example, Sun *et al.* prepared nitrogen-doped carbons with gradient N content and uniform pore structures, and through density functional theory (DFT) calculations, revealed that the introduction of nitrogen atoms onto the carbon surface strengthens CO_2 adsorption *via* enhanced dispersion and electrostatic interactions.[11] Wang *et al.* activated coal using trace amounts of alkali metal salt (K_2CO_3) and found that the resulting carbon exhibited short-range ordered microcrystalline structures and well-developed porosity, leading to superior CO_2 adsorption performance.[10]

However, understanding the roles of alkali metals and nitrogen during the actual preparation of carbon materials remains a significant challenge. Current consensus suggests that alkali metals primarily function as pore-forming agents,[14] while nitrogen dopants are responsible for modulating the electronic distribution of the carbon framework.[11] Residual alkali metal species (*e.g.*, –C–O–M moieties) are invariably retained within carbonaceous materials. These persistent components not only serve as pore-forming agents but also function as active sites that demonstrate the capacity to modulate electronic configurations. A pivotal yet underexplored aspect involves the synergistic electronic interactions between these alkali metal entities and strategically incorporated nitrogen dopants, which constitute the primary operational mechanism for enhanced CO_2 affinity. Notably, this paradigm remains incompletely understood at the atomic resolution level. Prevailing mechanistic models propose that KOH activation induces deconstruction of polymeric precursors into nanoscale carbon units, thereby generating amorphous microstructures while simultaneously facilitating oxygen functionalities elimination. This dual-phase transformation process establishes the structural prerequisites for optimized gas adsorption characteristics. During this process, potassium atoms spontaneously react with active oxygen radicals (O*) to form K–O species, which are anchored to the fragment edges in the form of C–O–K groups. This can be described by the reaction: K + O* + C → C–O–K.[13,15] Furthermore, studies have shown that the incorporation of alkali metal cations can alter the distribution and density of chemisorption sites.[12,16,17] Nevertheless, the mechanisms by which alkali metals influence CO_2 adsorption, and how their interactions with nitrogen dopants affect CO_2 capture performance, remain poorly understood. This is partly due to the inherent difficulties in precise experimental characterization, and partly attributable to the intrinsic structural complexity of coal-derived carbon materials.

To address these challenges, this study employs density functional theory (DFT) to systematically investigate the effects of alkali metals and nitrogen dopants on CO_2 adsorption in carbon-based materials. First, a series of carbon models were constructed and optimized, including typical nitrogen doping configurations (pyridinic, pyrrolic, graphitic, and amino types), alkali metal-doped carbons (K and Na), and co-doped systems combining both nitrogen and alkali metals. The CO_2 adsorption energies of these structures were subsequently calculated to quantitatively evaluate their adsorption capacities. The results indicate that CO_2 is physically adsorbed onto the material surfaces, with adsorption performance varying depending on the nitrogen doping type. Notably, alkali metal-doped systems exhibit significantly higher CO_2 adsorption capacities compared to nitrogen-doped counterparts, and the specific type of nitrogen dopant can further modulate the adsorption strength of CO_2 in the presence of alkali metals. To elucidate the underlying adsorption mechanisms, electrostatic potential mapping, energy decomposition analysis, and the Independent Gradient Model based on Hirshfeld partition (IGMH) were employed. These analyses revealed that, upon the introduction of alkali metals, electrostatic interactions become the dominant component of the weak interaction energy in the CO_2 adsorption process. In summary, this work uncovers the electronic effects of alkali metal activation in coal-derived carbon materials, demonstrating their role beyond mere pore-forming agents. It highlights the pivotal contribution of electrostatic interactions in CO_2 capture and provides mechanistic insight and theoretical guidance for the rational design of high-performance coal-based carbon adsorbents.

2. Computational methods

All calculations, including structural optimizations and electronic energy computations, were performed using the Gaussian 09 software package.[18] Geometry relaxations and frequency analyses of stationary points were conducted at the ωB97Xd/def2-SVP level,[19,20] while electronic energies were calculated at the ωB97Xd/def2-QZVP level.[19,20] For energy decomposition analysis, the SAPT0 method combined with the def2-TZVP basis set was employed using the PSI4 software.[21] This method ensures accuracy while defining elements up to the fourth period, thus reducing computational cost.[21] Electrostatic potential distribution on molecular surfaces, Mulliken population analysis and Independent Gradient Model based on Hirshfeld partition (IGMH) analyses were carried out with the Multiwfn program.[22–24]

The adsorption ability of catalysts toward CO_2 was quantitatively evaluated by the CO_2 adsorption energy (E_{ads}), calculated as follows:

$$E_{ads} = E_{*CO_2} - E_{*} - E_{CO_2} \quad (1)$$

where E_{*CO_2}, E_{*} and E_{CO_2} denote the electronic energies of CO_2 adsorbed on the carbon material, the bare carbon material, and isolated CO_2 molecule, respectively.

Intermolecular interaction energies were decomposed *via* symmetry-adapted perturbation theory (SAPT) calculations in PSI4. The interaction energy between molecular fragments can be expressed as:[21]

$$\Delta E_{SAPT} = \Delta E_{exc} + \Delta E_{ele} + \Delta E_{ind} + \Delta E_{dis} \quad (2)$$

where ΔE_{exc} is the exchange interaction term, representing exchange repulsion due to close proximity between fragments. A positive value indicates destabilization. ΔE_{ele} is the electrostatic interaction term, describing classical Coulomb interactions

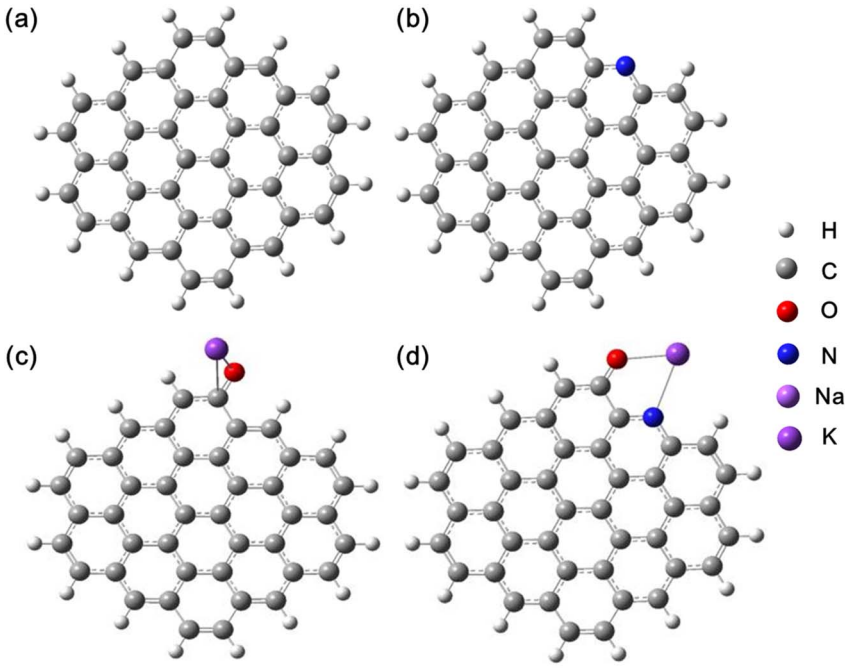

Fig. 1 Constructed carbon models with different doping configurations. (a) Pristine carbon model; (b) pyridinic nitrogen-doped carbon model; (c) potassium-doped carbon model; (d) co-doped carbon model with potassium and nitrogen.

between fragments; its value can be positive or negative. ΔE_{ind} is the induction (polarization) interaction term, which is negative and contributes attractively. ΔE_{dis} is the dispersion interaction term, reflecting charge polarization and charge transfer effects between fragments, also negative.

3. Results and discussion

3.1 Model construction

To investigate the interaction between alkali metal atoms and nitrogen atoms, a 14-carbon-ring armchair carbon cluster model was constructed to represent the pristine coal-based activated carbon, with hydrogen atoms terminating the cluster edges, as shown in Fig. 1a. This model features a relatively small dihedral angle (dias) value[25] and has been previously employed to study the effects of heteroatom doping on carbon materials.[11,26,27] It should be noted that coal and similar complex carbon materials possess intricate compositions; however, a simplified model is adopted here to focus primarily on the influence of heteroatoms. Regarding nitrogen atoms, their atomic size is nearly identical to that of carbon atoms, facilitating substitution and the formation of various doping configurations. In this study, pyridinic, pyrrolic, graphitic, and amine types were selected as representative nitrogen doping forms (Fig. 1b and S1). For alkali metal salts, during the co-pyrolysis process with carbon materials, a uniform molten environment is generated that promotes coal structure decomposition, cross-linking, and aromatization. The release of gaseous components from coal results in the formation of a porous activated carbon matrix with metal atoms loaded onto it. Among commonly used catalysts, alkali metals potassium (K) and sodium (Na) are the most active and exhibit superior catalytic performance, primarily existing in the material as –O–M (M = K, Na) structures formed *via* reactions. Accordingly, –O–K and –O–Na doped models were constructed, as illustrated in Fig. 1c and S2. Furthermore, based on these structures, co-doped models containing both nitrogen and alkali metals were established (Fig. 1d and S3).

3.2 Evaluation of adsorption performance

To evaluate the CO_2 adsorption capacity of the above structures, we further calculated the CO_2 adsorption energy (calculation method detailed in eqn (1)), which quantitatively assesses the catalyst's ability to adsorb CO_2. Fig. 2a shows a stable snapshot of CO_2 adsorbed on the pristine, undoped carbon model. It can be observed that the CO_2 molecule lies parallel to the carbon surface, indicating a physical adsorption mode. The adsorption energy is -3.17 kJ mol^{-1}, which is negative, suggesting that CO_2 adsorption is thermodynamically favorable. The shortest distance between the CO_2 molecule and the carbon structure is 2.66 Å, demonstrating structural stability of the physical adsorption at the edge of the carbon model. This is consistent with Qu *et al.*'s findings on SO_2 adsorption[28] and aligns with the CO_2 adsorption behavior reported by Sun *et al.*,[11] that is, the adsorption of SO_2 and CO_2 at the carbon edge is thermodynamically heat-resistant.

Furthermore, we calculated the CO_2 adsorption energies for nitrogen-doped carbon materials (with doping types including pyridinic N, amino N, graphitic N, and pyrrolic N, denoted as Pd_N, A_N, G_N, and Pr_N respectively, shown in Fig. 2b), potassium/sodium-doped carbon (denoted as K and Na), as well as their co-doped systems with nitrogen (Fig. 2c and d). Fig. 2b

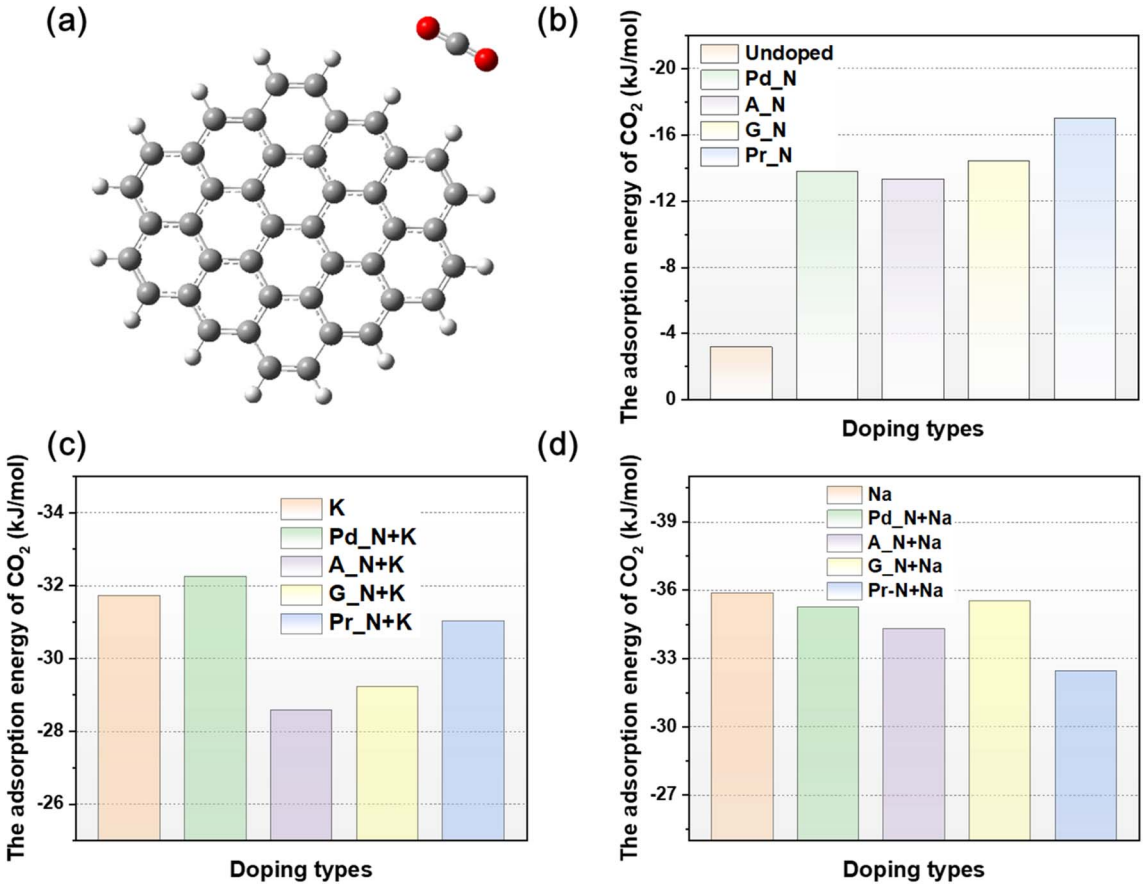

Fig. 2 Summary of CO_2 adsorption energies for various doped carbon models. (a) Optimized structure of CO_2 adsorbed on undoped carbon; (b) CO_2 adsorption energies of different types of N-doped carbons compared to undoped carbon; (c) CO_2 adsorption energies of N and K co-doped carbons compared to K-doped carbon; (d) CO_2 adsorption energies of N and Na co-doped carbons compared to Na-doped carbon.

first presents a comparison of CO_2 adsorption energies between various nitrogen-doped carbons and the pristine undoped carbon. It is evident that doping nitrogen significantly enhances the CO_2 adsorption capacity compared to the undoped carbon, with adsorption energies ranging from −17 to −13 kJ mol^{-1}. The strength of adsorption decreases in the order: pyrrolic N (E_{ads} = −17.00 kJ mol^{-1}) > graphitic N (E_{ads} = −14.41 kJ mol^{-1}) > pyridinic N (E_{ads} = −13.76 kJ mol^{-1}) ≈ amino N (E_{ads} = −13.32 kJ mol^{-1}) ≫ pristine graphite carbon (E_{ads} = −3.17 kJ mol^{-1}). These results are consistent with Qu *et al.*'s findings on SO_2 adsorption (N can enhance SO_2 physisorption at the carbon edge)[28] and aligns with the CO_2 adsorption behavior reported by Sun *et al.* (the introduction of N atoms into carbon surfaces could greatly enhance the CO_2 adsorption).[11]

Fig. 3 illustrates the detailed configurations and adsorption behavior of CO_2 on various nitrogen-doped carbon models. It was observed that CO_2 tends to adsorb on the side of pyridinic N, nearly coplanar with the carbon basal plane; on amino-doped carbon, CO_2 adsorbs predominantly above the amino group, almost parallel to the carbon plane. For graphitic N and pyrrolic N doped structures, CO_2 preferentially adsorbs parallel to the carbon basal plane surrounding the nitrogen atom. Different functional groups influence CO_2 adsorption differently, reflected also in varying distances between the CO_2 molecule and the adsorbent. Specifically, the distance between the C atom in CO_2 and the N atom in the carbon structure follows the trend: amino N (2.884 Å) < pyridinic N (3.083 Å) < pyrrolic N (3.826 Å) < graphitic N (3.946 Å).

The effect of alkali metal doping on carbon materials is a key focus of our study. We investigated both alkali metal single doping and co-doping with nitrogen. First, the impact of K/Na single doping on carbon materials was analyzed. Fig. S5 illustrates the specific behavior of CO_2 adsorption on K/Na-doped carbon models. Compared to the original graphite carbon surface (−3.17 kJ mol^{-1}), the adsorption capacity is significantly increased, with Na doping (−35.88 kJ mol^{-1}) showing a lower adsorption energy than K doping (−31.72 kJ mol^{-1}). Both values greatly exceed those of nitrogen-doped carbons (−17 to −13 kJ mol^{-1}), indicating a marked enhancement in adsorption capability. When nitrogen atoms are further introduced based on alkali metal doping (Fig. 2c and d), the adsorption behavior varies with the types of alkali metals and nitrogen dopants. Regardless, the CO_2 adsorption capacity remains substantially stronger than that of carbons doped solely with non-metal elements. Fig. S6 details the adsorption energies and

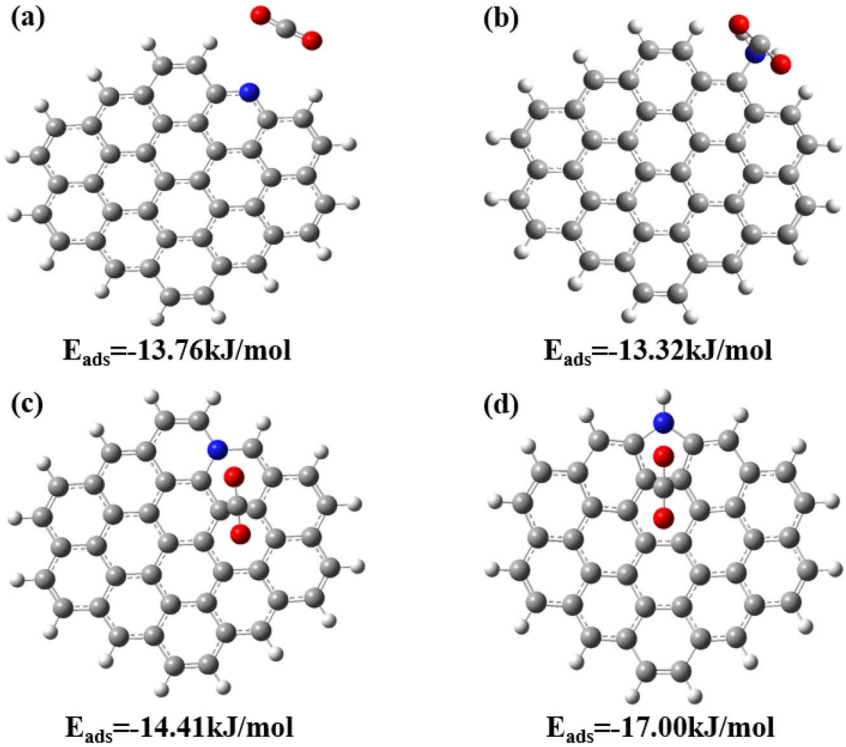

Fig. 3 CO_2 adsorption configuration and adsorption energy on nitrogen-doped carbon surface (a) pyridine nitrogen; (b) amino group; (c) graphite nitrogen; (d) pyrrole nitrogen.

configurations of CO_2 on activated carbon surfaces bearing –C–O–K structures combined with nitrogen functional groups. CO_2 is adsorbed parallel to the carbon plane in pyridinic N and –C–O–K synergistic configurations as well as amine and –C–O–K combinations. In contrast, CO_2 adsorbs at certain angles relative to the carbon plane in graphite N–K and pyrrolic N–K co-doped structures.

Different functional groups exert distinct effects on CO_2 adsorption, mainly due to interactions between the oxygen atoms in CO_2 and the potassium atoms in the –C–O–K groups. The O–K distances vary slightly among configurations: pyridinic N (2.822 Å) > pyrrolic N (2.742 Å) > amine (2.735 Å) > graphite N (2.732 Å). Overall, nitrogen functional groups show both inhibitory and promotional effects on the graphite carbon models containing –C–O–K groups. Pyridinic N slightly enhances adsorption performance, decreasing adsorption energy by 0.53 kJ mol^{-1}. Conversely, graphite N and amine groups weaken adsorption, with the amine group causing the largest reduction of 3.14 kJ mol^{-1}. Similarly, Fig. S7 presents CO_2 adsorption energies and configurations on activated carbon surfaces with –C–O–Na groups combined with nitrogen functional groups. The synergy between graphite N, pyridinic N and Na shows minimal influence on adsorption. However, amine and pyrrolic N groups weaken adsorption, with pyrrolic N causing the greatest reduction of 3.41 kJ mol^{-1}.

Based on the above analysis, we can gain a clearer understanding of the interaction between alkali metal atoms and nitrogen atoms on the performance of carbon materials. Alkali metals can significantly enhance the CO_2 adsorption capacity of carbon materials, broadening our understanding of their role beyond merely creating pores to increase surface area—they also improve the CO_2 adsorption activity. To gain deeper insight into the underlying mechanism, we further analyzed the electrostatic potential (ESP) distribution of the aforementioned carbon structures. It should be noted that our calculations assume ideal dry conditions. In practical applications, the hydrophilic nature of alkali metal sites may lead to competitive adsorption by water molecules, potentially reducing CO_2 capture efficiency. Future work will explore surface modifications or hydrophobic coatings to mitigate this issue.[29]

3.3 Electrostatic potential analysis

Fig. 4a shows the ESP distribution on the surface of the pristine, undoped activated carbon. The potential is relatively uniform, with the highest values located at the edge hydrogen atoms, while the carbon basal plane exhibits a smooth and moderate ESP. For nitrogen-doped carbon surfaces (*e.g.*, Fig. 4b and S8), significant changes in ESP occur near the doping sites. On the pyridinic N-doped carbon surface (Fig. 4b), the maximum ESP appears at the edge hydrogen atoms of the carbon structure, whereas the minimum ESP is localized at the doped nitrogen atom, with a relatively smooth ESP across the basal plane. In the pyrrolic N-doped carbon surface (Fig. S9b), the maximum ESP is found at the edge adjacent to the pyrrolic nitrogen. The introduction of the nitrogen atom enhances local electronegativity, resulting in a reduced ESP near the doping site, with the minimum ESP located on the basal plane, which remains

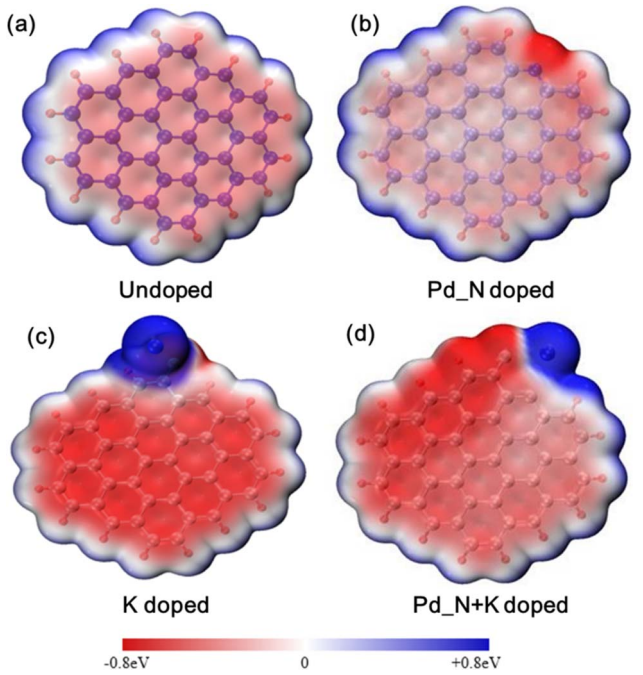

Fig. 4 Electrostatic potential (ESP) distributions of differently doped carbon models. (a) Pristine (undoped) carbon; (b) pyridinic nitrogen-doped carbon; (c) potassium-doped carbon; (d) co-doped carbon with pyridinic nitrogen and potassium.

relatively smooth overall. For amine-doped carbon (Fig. S9c), the maximum ESP appears at the hydrogen atom of the amine group, and the minimum is at the nitrogen atom. This is attributed to electron transfer from the hydrogen atoms to the nitrogen atom within the amine group, causing elevated ESP at the H sites and lowered ESP at the N site, while the basal plane ESP remains smooth. On the graphite N-doped carbon surface (Fig. S9d), the maximum ESP occurs at the doped nitrogen atom and also at the edge hydrogen atoms. The basal plane shows a generally smooth ESP distribution, with increased ESP near the doped graphite nitrogen and decreased ESP in adjacent regions. This detailed ESP mapping reveals how nitrogen doping modifies the local electronic environment of carbon materials, which plays a crucial role in modulating their interaction with CO_2 molecules.

Fig. 4c presents the electrostatic potential (ESP) distribution on the surface of potassium-doped carbon. Due to the stronger electron-donating ability of alkali metals, the ESP extrema on the potassium-doped surface are significantly higher than those on the pristine carbon surface. The introduction of potassium creates a pronounced ESP maximum at the dopant site (K atom), while simultaneously lowering the ESP across the carbon basal plane. The sodium-doped surface shows a similar ESP distribution pattern to that of potassium doping, with an ESP maximum appearing at the Na atom and a reduced ESP on the carbon basal plane. The interaction between doped potassium or sodium on the activated carbon surface and CO_2 is characterized by the positively charged metal atoms acting as basic sites, which enhance CO_2 adsorption by accepting electron density from the oxygen atoms of CO_2 molecules. Additionally, the carbon atom in CO_2 is attracted by negatively charged atoms on the carbon surface, further strengthening CO_2 adsorption. Overall, the incorporation of Na and K into the activated carbon surface results in the strongest affinity for CO_2 capture.

A further analysis was conducted on the electrostatic potential (ESP) distribution of co-doped systems with alkali metals and nitrogen atoms (Fig. 4d, S9 and S10). On the surface with the synergistic effect of pyridinic nitrogen and the carbon–oxygen–potassium (C–O–K) structure (Fig. 4d), the ESP on the carbon basal plane is reduced. A minimum ESP value appears at the nitrogen atom of the doped pyridinic nitrogen, while a maximum ESP is found at the potassium atom. Due to potassium's tendency to lose electrons and become positively charged, it exhibits a high electrostatic potential. The locations of these ESP extrema closely correspond to the CO_2 adsorption sites, indicating that electrostatic interactions significantly influence CO_2 adsorption on the K and pyridinic nitrogen co-doped activated carbon surface. Similarly, on the surface with pyrrolic nitrogen and C–O–K synergy (Fig. S9b), the carbon basal plane shows a decreased ESP, with a maximum at the K atom and a minimum at the O atom. Comparable patterns are also observed on other co-doped surfaces (Fig. S9 and S10).

Furthermore, to gain in-depth theoretical insight into the contributions of individual atoms—particularly alkali metal atoms—to the charge distribution in our models, we performed Mulliken population analysis, as summarized in Fig. S11–S15. Fig. S11 illustrates the Mulliken analysis for carbon models with single alkali metal (K, Na) doping. It reveals that alkali metal atoms carry highly positive charges (0.781 atomic units (a.u.) for K, 0.761 a.u. for Na), while oxygen atoms adjacent to the alkali metals host strongly negative charges (−0.530 a.u. for O in K–O, −0.554 a.u. for O in Na–O). The charge difference between K and O is 1.311 a.u.—smaller than that in the Na–O structure (1.315 a.u.). This discrepancy may induce a stronger electrostatic potential field near Na–O sites, thereby enhancing CO_2 adsorption energy. Fig. S12–S15 present Mulliken analysis results for carbon models doped with amino, graphitic, pyridinic, or pyrrolic nitrogen—both individually and in synergy with alkali metals. Collectively, these data demonstrate the profound impact of alkali metal incorporation on atomic charge distribution in the materials. Purely nitrogen-doped models exhibit faint surface coloring, indicating small, uniformly distributed surface atomic charges. Upon introducing alkali metals (K, Na), however, the charge distribution becomes extremely polarized at C–O–K/Na interfaces: oxygen atoms acquire negative charges, while alkali metals bear positive charges with magnitudes far exceeding those of other non-metallic elements. Meanwhile, consistent with the pure alkali metal-doped models, charge differences in Na–O structures are generally larger than those in K–O structures. This suggests stronger electrostatic forces near Na–O sites, which are likely more favorable for CO_2 adsorption.

In summary, the above analysis indicates that co-doping with alkali metals and nitrogen functional groups induces significant changes in the electronic structure of the carbon surface. Generally, nitrogen functional group doping lowers the

Table 1 Energy decomposition analysis of CO_2 adsorption on pristine activated carbon and nitrogen-doped surfaces (kJ mol^{-1})

Model	ΔE_{ele}	ΔE_{exc}	ΔE_{ind}	ΔE_{dis}	ΔE_{total}
Pristine (undoped) carbon	−2.093	6.754	−0.832	−8.000	−4.171
Pyridinic nitrogen-doped surface	−31.188	31.631	−4.908	−16.049	−20.514
Pyrrolic nitrogen-doped surface	−10.139	22.985	−2.970	−30.579	−20.703
Graphitic nitrogen-doped surface	−7.765	23.194	−3.569	−28.306	−16.445
Amine-doped surface	−22.361	27.283	−3.824	−18.240	−17.141

electrostatic potential of the carbon basal plane, while the maximum electrostatic potential appears at the potassium atom and the minimum near the nitrogen functional groups. The location of the maximum electrostatic potential closely corresponds to the final CO_2 adsorption sites, suggesting that electrostatic interactions play a crucial role in CO_2 adsorption on activated carbon surfaces co-doped with potassium and nitrogen. Mulliken population analysis reveals that the introduction of alkali metals (K, Na) into carbon models leads to increased charge distribution heterogeneity. Notably, the atomic charge disparity in Na–O structures exceeds that in K–O configurations, thereby generating stronger electrostatic interactions around these sites. This enhanced electrostatic environment promotes more efficient CO_2 adsorption performance.

3.4 Energy decomposition analysis

Based on the electrostatic potential distribution, it is evident that electrostatic interactions significantly influence the CO_2 adsorption process on nitrogen-functionalized surfaces as well as in synergy with alkali metals. To further elucidate this, we performed energy decomposition analysis (method details are provided in the SI) to compare the specific physical components of weak interactions across different configurations. According to perturbation theory, the interaction energy is divided into four components: electrostatic, exchange, dispersion, and induction (Tables 1–3). Table 1 presents the energy decomposition of CO_2 adsorption on pristine activated carbon and nitrogen-doped surfaces. It can be seen that for the pristine undoped carbon surface, dispersion interactions (ΔE_{dis}) constitute the major part of the adsorption energy. For pyrrolic and graphitic nitrogen-doped surfaces, ΔE_{dis} dominate over electrostatic interactions (ΔE_{ele}), whereas for pyridinic and amine nitrogen-doped surfaces, ΔE_{dis} are weaker than ΔE_{ele}. These results indicate that the type of nitrogen dopant can modulate the nature of the interaction forces, thereby affecting the CO_2 adsorption capacity. Meanwhile, it is evident that regardless of the nitrogen species, the ΔE_{dis} and ΔE_{ele} values for N-doped carbons are both higher than those of pristine carbon. This indicates that nitrogen enhances CO_2 adsorption by leveraging these two types of interaction forces.

Tables 2 and 3 present the energy decomposition analysis of CO_2 adsorption on alkali metal-doped surfaces and those co-doped with nitrogen. It is evident that in doping systems containing alkali metals, the electrostatic interaction (ΔE_{ele}) accounts for the largest proportion. For instance, in the pyridinic nitrogen and potassium co-doped surface (Table 2), the electrostatic interaction is the dominant component of the interaction energy, and the synergistic electrostatic interaction is stronger than that of nitrogen doping alone. Moreover, the energy decomposition results indicate that the synergistic effect between pyridinic nitrogen and the potassium group leads to higher electrostatic and total interaction energies compared to potassium doping alone. These findings are consistent with the electrostatic potential distribution analysis of various doped models shown in Fig. 3, demonstrating that the enhanced CO_2 adsorption performance upon alkali metal introduction is primarily attributed to the increased electrostatic component of the weak interactions.

3.5 Independent gradient model based on Hirshfeld partition (IGMH) analysis

Furthermore, we employed the Independent Gradient Model based on Hirshfeld partition (IGMH) to visually represent both inter-fragment and intra-fragment interactions, as shown in Fig. 4 and S16–S20. IGMH utilizes the three-dimensional function δ to intuitively display the interaction regions between atoms. Peaks in δ occur in regions where the electron densities of two atoms overlap, indicating the presence of atomic

Table 2 Energy decomposition analysis of CO_2 adsorption on potassium-doped and nitrogen–potassium co-doped surfaces (kJ mol^{-1})

Model	ΔE_{ele}	ΔE_{exc}	ΔE_{ind}	ΔE_{dis}	ΔE_{total}
Potassium-doped surface	−71.526	63.663	−19.764	−22.780	−50.408
Pyridinic nitrogen and potassium co-doped surface	−77.802	66.345	−20.652	−22.842	−54.951
Pyrrolic nitrogen and potassium co-doped surface	−63.618	53.962	−15.609	−22.449	−47.715
Graphitic nitrogen and potassium co-doped surface	−48.669	42.443	−11.296	−20.587	−38.119
Amine and potassium co-doped surface	−62.723	56.953	−15.845	−27.545	−49.161

Table 3 Energy decomposition of CO_2 adsorption on sodium-doped and nitrogen–sodium co-doped surfaces (kJ mol^{-1})

Model	ΔE_{ele}	ΔE_{exc}	ΔE_{ind}	ΔE_{dis}	ΔE_{total}
Sodium-doped surface	−73.104	60.424	−20.573	−17.667	−50.920
Pyridinic nitrogen and sodium co-doped surface	−60.530	51.801	−16.014	−15.642	−40.385
Pyrrolic nitrogen and sodium co-doped surface	−67.546	56.798	−18.755	−18.889	−48.391
Graphitic nitrogen and sodium co-doped surface	−55.210	43.975	−14.011	−16.634	−41.880
Amino group and sodium co-doped surface	−70.286	58.443	−19.261	−17.704	−48.808

interactions. Under the equilibrium molecular structure, larger density overlap between atoms corresponds to higher δ peaks, which implies stronger atomic interactions and consequently shorter interatomic distances.

Fig. 5a presents the IGMH analysis of CO_2 adsorbed on the pristine, undoped carbon surface. The δ_g isosurface is mainly concentrated between the CO_2 molecule and the original activated carbon surface. The isosurface predominantly appears green, indicating that the intermolecular interaction at this stage is mainly dispersive (van der Waals) interaction. In the left panel, the molecular coloring evaluates each atom's contribution to the interaction between the two fragments: atoms with greater contributions are colored redder, while those with smaller contributions appear bluer. From the atomic colors, it can be seen that the carbon atom in CO_2 contributes the most, while the two edge hydrogen atoms and adjacent carbon atoms in the carbon structure also contribute. In the right panel, two peaks appear at sign(λ^2)ρ values of approximately −0.005 a.u. and +0.005 a.u., characteristic of van der Waals interactions, which occur in regions of low electron density where the sign of λ^2 fluctuates between positive and negative. Fig. 5b shows the isosurface primarily concentrated between CO_2 and the pyridinic nitrogen-doped carbon plane, with a shape closely matching the CO_2 molecule. The isosurface is mainly green and predominantly contributed by the pyridinic nitrogen atom and its five connected chain-like carbon atoms. For the pyridinic nitrogen-doped configuration, a main peak is observed around −0.01 a.u., indicating that hydrogen bonding dominates the electrostatic interaction. Another peak at +0.005 a.u. reflects the influence of van der Waals forces.

In Fig. 5c, there is a strong electrostatic interaction between the carbon atoms of CO_2 and the potassium (K) atom on the K-doped activated carbon surface. From the color-coded image on the left, the main contributors are the oxygen atoms and the K atom, as well as the carbon atom in the CO_2 molecule. The scatter plot on the right shows a peak near sign(λ^2)ρ = −0.02 a.u., corresponding to the blue-green region on the isosurface map, while a sharp peak around sign(λ^2)ρ = +0.01 a.u. indicates the presence of exchange repulsion that prevents CO_2 from approaching the adsorbent too closely. In the pyridinic nitrogen and K co-doped configuration (Fig. 5d), a peak appears at about −0.02 a.u., corresponding to the symmetric blue-green

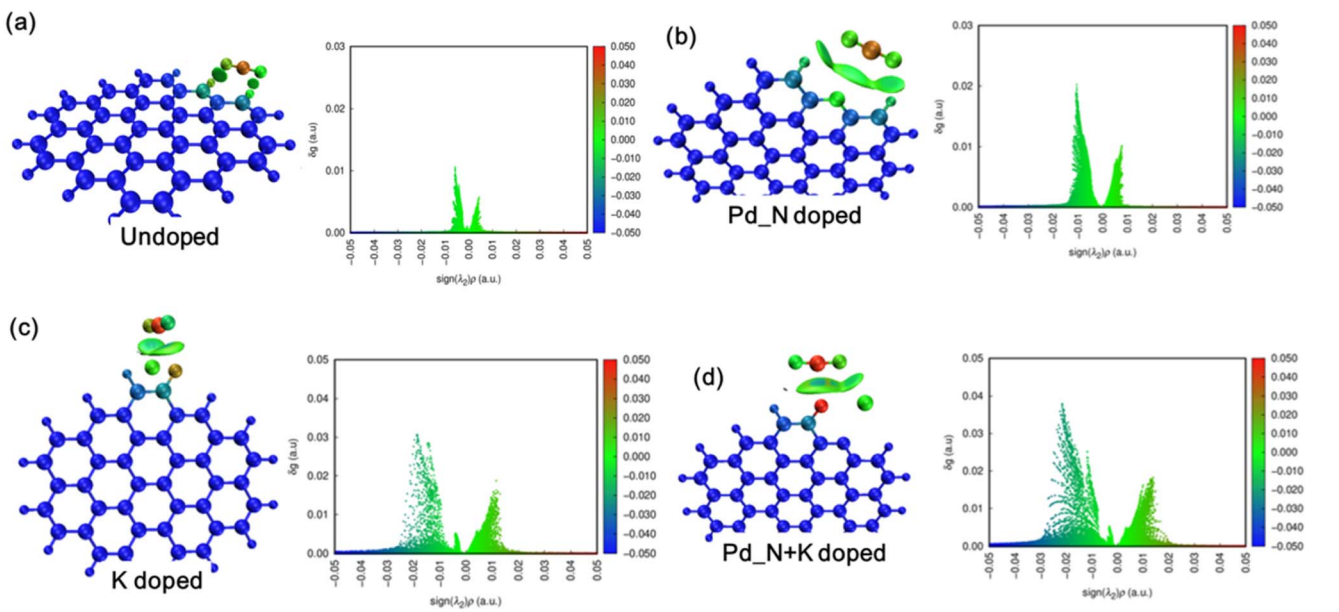

Fig. 5 IGMH analysis of CO_2 adsorption on surfaces of different doped carbon models. (a) Undoped carbon; (b) pyridinic nitrogen-doped carbon; (c) potassium-doped carbon; (d) pyridinic nitrogen and potassium co-doped carbon.

isosurface between the pyridinic nitrogen and CO_2 in the scatter plot. This interaction is mainly contributed by the –C–O–K group and the carbon atom in CO_2, indicating that electrostatic interaction dominates the interaction energy. The area of the isosurface and the peak is significantly larger than that of pyridinic nitrogen doping alone, demonstrating that the synergy between the –C–O–K group and pyridinic nitrogen greatly enhances CO_2 adsorption. Through these analyses, we further confirm that the electrostatic interaction plays a particularly critical role in the synergistic effect between alkali metals and nitrogen.

The above theoretical studies which systematically investigates the influence of alkali metals on CO_2 adsorption have revealed the indispensable role of alkali metals in enhancing CO_2 adsorption performance. However, practical applications require addressing critical factors such as material humidity (microscopic water molecule presence) and structural evolution under operational conditions. Future research should employ realistic simulations and atomic-level characterization techniques to further decouple these complex interactions.

4. Conclusions

In summary, this study systematically elucidates the synergistic mechanism of alkali metal (K/Na) activation and nitrogen doping on CO_2 adsorption in coal-based carbon materials using density functional theory (DFT). We found that alkali metal doping, primarily in the form of –C–O–M (M = K, Na) structures, is the key factor for enhancing CO_2 adsorption performance. The introduction of K/Na significantly strengthens adsorption, increasing the adsorption energy from -3.17 kJ mol^{-1} for pristine carbon to -35.88 kJ mol^{-1} (Na) and -31.72 kJ mol^{-1} (K), far exceeding that of single nitrogen doping systems (-17 to -13 kJ mol^{-1}). The type of nitrogen doping regulates the adsorption behavior: pyrrolic and graphitic nitrogen-doped carbons are dominated by dispersion interactions, favoring parallel adsorption of CO_2 on the carbon basal plane; whereas pyridinic nitrogen and amino groups attract CO_2 to edge sites *via* electrostatic interactions. In synergistic systems, compared to single K doping, pyridinic nitrogen and K co-doping further decreases adsorption energy by 0.53 kJ mol^{-1}. In contrast, amino and pyrrolic nitrogen weaken the alkali metal's enhancement effect, increasing adsorption capacity by 3.14–3.41 kJ mol^{-1}.

Further mechanistic analysis revealed that alkali metal doping creates localized high electrostatic potential regions at K/Na sites on the carbon surface, while nitrogen atoms—especially pyridinic nitrogen—induce low electrostatic potential zones. Together, they generate a strong electrostatic potential gradient field. This gradient facilitates a pronounced electrostatic attraction between the positively charged metal sites (K^+/Na^+) and the electron-rich oxygen atoms of CO_2, substantially enhancing adsorption. Mulliken population analysis further demonstrates that the introduction of alkali metals induces a more heterogeneous atomic charge distribution on the carbon model surface, leading to enhanced electrostatic potential fields. Energy decomposition analysis (EDA) confirmed that electrostatic interaction energy (ΔE_{ele}) dominates over 60% of the total interaction energy in alkali metal doped systems (*e.g.*, for K doping, $\Delta E_{ele} = -71.526$ kJ mol^{-1}, accounting for 70% of total interaction energy); in the pyridinic nitrogen + K co-doped system, ΔE_{ele} further decreases to -77.802 kJ mol^{-1}, highlighting that electrostatic synergy underpins the cooperative enhancement effect. Independent Gradient Model based on Hirshfeld partition (IGMH) analysis visually demonstrated that co-doping of pyridinic nitrogen and K significantly enlarges the electrostatic interaction region between CO_2 and the adsorbent, with a notable increase in isosurface peak area, corroborating the strengthening of electrostatic interactions. It is noteworthy that this work focuses on theoretical insights into the influence of alkali metals on CO_2 adsorption. For future investigations, it will be essential to consider additional factors such as competitive water adsorption and achieve atomic-level experimental understanding through advanced *in situ* characterization techniques.

This work reveals at the atomic scale the electronic effects of alkali metals beyond their conventional role as "pore formers," clarifies the central role of electrostatic interactions in CO_2 adsorption, and provides a theoretical foundation for the design of high-performance coal-based carbon adsorbents.

Conflicts of interest

There are no conflicts to declare.

Data availability

Data available on request from the authors. The data that support the findings of this study are available from the corresponding author, mengxiaoxiao@hit.edu.cn, upon reasonable request.

Supplementary information is available. See DOI: **https://doi.org/10.1039/d5ra06428g**.

References

1 C. Corvalán, S. Hales and A. J. McMichael, *Ecosystems and Human Well-Being : Health Synthesis : a Report of the Millennium Ecosystem Assessment*, WHO, 2006.
2 P. Friedlingstein, M. O'Sullivan, M. W. Jones, *et al.*, Global Carbon Budget 2023, *Earth Syst. Sci. Data*, 2023, **15**(12), 5301–5369.
3 J. D. Shakun, P. U. Clark, F. He, S. A. Marcott, A. C. Mix, Z. Liu, B. Otto-Bliesner, A. Schmittner and E. Bard, Global warming preceded by increasing carbon dioxide concentrations during the last deglaciation, *Nature*, 2012, **484**(7392), 49–54.
4 T. M. Letcher, *Future Energy: Improved, Sustainable and Clean Options for Our Planet*, Elsevier, 2020, pp. 3–17.
5 J. W. B. Rae, Y. G. Zhang, X. Liu, G. L. Foster, H. M. Stoll and R. D. M. Whiteford, Atmospheric CO_2 over the Past 66 Million Years from Marine Archives, *Annu. Rev. Earth Planet. Sci.*, 2025, **18**, 609–650.

6 P. Fennell, J. Driver, C. Bataille and S. J. Davis, Going net zero for cement and steel, *Nature*, 2022, **603**, 574–577.
7 S. Liu, L. Wang, H. Zhang, H. Fang, X. Yue, S. Wei, S. Liu, Z. Wang and X. Lu, Efficient CO_2 Capture and Separation in MOFs: Effect from Isoreticular Double Interpenetration, *ACS Appl. Mater. Interfaces*, 2024, **16**(6), 7152–7160.
8 J. D. V. Souza-Filho, E. S. Oliveira, J. B. Guedes, J. B. A. Silva Júnior, C. R. F. Alves, J. A. Coelho, A. C. A. Lima, M. Bastos-Neto, J. M. Sasaki, F. S. B. Mota, A. R. Loiola and B. V. Elsevier, Zeolite A grown on fiberglass: A prominent CO_2 adsorbent for CO_2/CH_4 separation, *Colloids Surf., A*, 2024, **683**, 132952.
9 H. He, R. Zhang, P. Zhang, P. Wang, N. Chen, B. Qian, L. Zhang, J. Yu and B. Dai, Functional Carbon from Nature: Biomass-Derived Carbon Materials and the Recent Progress of Their Applications, *Adv. Sci.*, 2023, **10**, 202205557.
10 L. Wang, F. Sun, F. Hao, Z. Qu, J. Gao, M. Liu, K. Wang, G. Zhao and Y. Qin, A green trace K_2CO_3 induced catalytic activation strategy for developing coal-converted activated carbon as advanced candidate for CO_2 adsorption and supercapacitors, *Chem. Eng. J.*, 2020, **383**, 123205.
11 F. Sun, X. Liu, J. Gao, X. Pi, L. Wang, Z. Qu and Y. Qin, Highlighting the role of nitrogen doping in enhancing CO_2 uptake onto carbon surfaces: a combined experimental and computational analysis, *J. Mater. Chem. A*, 2016, **4**(47), 18248–18252.
12 J. E. Eichler, J. N. Burrow, N. Katyal, G. Henkelman and C. B. Mullins, Modulation of CO_2 adsorption thermodynamics and selectivity in alkali-carbonate activated N-rich porous carbons, *J. Mater. Chem. A*, 2023, **11**(24), 12811–12826.
13 F. Yuan, Z. Wu, Z. Li, Q. Sun, Q. Wang, R. Li, W. Wang, D. Zhang and B. Wang, Decoupling KOH Activation Path to Construct Graphitic Porous Carbon Anode for Enhanced Potassium Ion Storage, *Small*, 2025, **21**, 2505910.
14 A. Memetova, I. Tyagi, L. Singh, R. R. Karri, Suhas, *et al.*, Nanoporous carbon materials as a sustainable alternative for the remediation of toxic impurities and environmental contaminants: A review, *Sci. Total Environ.*, 2022, **838**, 155943.
15 Q. Lu, R. Guo, H. Zhang, J. P. Wang, T. Lu, G. Y. Li and Y. H. Liang, To stimulate, and to inhibit: A theoretical understanding of the sodium-catalytic mechanism of coke gasification, *Chem. Eng. J.*, 2022, **435**, 135091.
16 D. Iruretagoyena, X. Huang, M. S. P. Shaffer and D. Chadwick, Influence of Alkali Metals (Na, K, and Cs) on CO_2 Adsorption by Layered Double Oxides Supported on Graphene Oxide, *Ind. Eng. Chem. Res.*, 2015, **54**(46), 11610–11618.
17 Q. Li, W. Xu, X. Liang, B. Liu, Q. Wu, Z. Zeng, L. Li and X. Ma, Specific alkali metal sites as CO_2 traps in activated carbon with different pore size for CO_2 selective adsorption: GCMC and DFT simulations, *Fuel*, 2022, **325**(1), 124871.
18 M. J. Frisch, G. W. Trucks, H. B. Schlegel, G. E. Scuseria, M. A. Robb, J. R. Cheeseman, G. Scalmani, V. Barone, B. Mennucci, G. A. Petersson, H. Nakatsuji, M. Caricato, X. Li, H. P. Hratchian, A. F. Izmaylov, J. Bloino, G. Zheng, J. L. Sonnenberg, M. Hada, M. Ehara, K. Toyota, R. Fukuda, J. Hasegawa, M. Ishida, T. Nakajima, Y. Honda, O. Kitao, H. Nakai, T. Vreven, J. A. Montgomery Jr., J. E. Peralta, F. Ogliaro, M. Bearpark, J. J. Heyd, E. Brothers, K. N. Kudin, V. N. Staroverov, T. Keith, R. Kobayashi, J. Normand, K. Raghavachari, A. Rendell, J. C. Burant, S. S. Iyengar, J. Tomasi, M. Cossi, N. Rega, J. M. Millam, M. Klene, J. E. Knox, J. B. Cross, V. Bakken, C. Adamo, J. Jaramillo, R. Gomperts, R. E. Stratmann, O. Yazyev, A. J. Austin, R. Cammi, C. Pomelli, J. W. Ochterski, R. L. Martin, K. Morokuma, V. G. Zakrzewski, G. A. Voth, P. Salvador, J. J. Dannenberg, S. Dapprich, A. D. Daniels, O. Farkas, J. B. Foresman, J. V. Ortiz, J. Cioslowski and D. J. Fox, *Gaussian 09, Revision D.01*, Gaussian, Inc., Wallingford, CT, 2013.
19 J. D. Chai and M. Head-Gordon, Long-range corrected hybrid density functionals with damped atom-atom dispersion corrections, *Phys. Chem. Chem. Phys.*, 2008, **10**(44), 6615–6620.
20 F. Weigend and R. Ahlrichs, Balanced basis sets of split valence, triple zeta valence and quadruple zeta valence quality for H to Rn: Design and assessment of accuracy, *Phys. Chem. Chem. Phys.*, 2005, **7**(18), 3297–3305.
21 D. G. A. Smith, L. A. Burns, A. C. Simmonett, *et al.*, PSI4 1.4: open-source software for high-throughput quantum chemistry, *J. Chem. Phys.*, 2020, **152**(18), 184108.
22 T. Lu and F. Chen, Multiwfn: A multifunctional wavefunction analyzer, *J. Comput. Chem.*, 2012, **33**(5), 580–592.
23 T. Lu, A comprehensive electron wavefunction analysis toolbox for chemists, Multiwfn, *J. Chem. Phys.*, 2024, **161**, 082503.
24 T. Lu and Q. Chen, Independent gradient model based on Hirshfeld partition: A new method for visual study of interactions in chemical systems, *J. Comput. Chem.*, 2022, **43**(8), 539–555.
25 L. Xie, W. Zhou, Z. Qu, Y. Ding, J. Gao, F. Sun and Y. Qin, Understanding the activity origin of oxygen-doped carbon materials in catalyzing the two-electron oxygen reduction reaction towards hydrogen peroxide generation, *J. Colloid Interface Sci.*, 2022, **610**, 934–943.
26 Z. Liu, X. Fu, M. Li, F. Wang, Q. Wang, G. Kang and F. Peng, Novel silicon-doped, silicon and nitrogen-codoped carbon nanomaterials with high activity for the oxygen reduction reaction in alkaline medium, *J. Mater. Chem. A*, 2015, **3**(7), 3289–3293.
27 R. A. Sidik, A. B. Anderson, N. P. Subramanian, S. P. Kumaraguru and B. N. Popov, O_2 reduction on graphite and nitrogen-doped graphite: Experiment and theory, *J. Phys. Chem. B*, 2006, **110**(4), 1787–1793.
28 Z. Qu, F. Sun, X. Liu, J. Gao, Z. Qie and G. Zhao, The effect of nitrogen-containing functional groups on SO_2 adsorption on carbon surface: Enhanced physical adsorption interactions, *Surf. Sci.*, 2018, **677**, 78–82.
29 L. Chen, H. Xiong, D. Zhang, B. Xie, Z. Ni and S. Xia, CO_2 adsorption and dissociation performance of metal-doped h-BN: A DFT study on the electronic-geometric synergistic effect, *Mol. Catal.*, 2025, **585**, 115330.